PNAS RESEARCH ARTICLE | APPLIED PHYSICAL SCIENCES

Direct optical observation of solid electrolyte interphase formation dynamics in lithium-ion batteries

Wenlong Li[a,1], Tianxiao Sun[a,1], Sameep Rajubhai Shah[b,1], Zhengyu Ju[a], Jigang Zhou[c], Kejie Zhao[b,2], Guihua Yu[a,2], and Yijin Liu[a,2]

Affiliations are included on p. 9.

Edited by David Weitz, Harvard University, Cambridge, MA; received November 5, 2025; accepted February 1, 2026

Lithium-ion battery formation is a pivotal step that dictates performance, longevity, and manufacturing safety. At the core of this process is the formation and evolution of the solid electrolyte interphase (SEI), whose nanoscale thickness, high environmental sensitivity, and dynamic behavior have long hindered direct characterization. Here, we exploit the SEI-induced refractive index matching effect and utilize operando optical microscopy to directly visualize SEI growth in real time. Our observations reveal pronounced lateral heterogeneity and asynchronicity during the first lithiation of graphite anodes. Surprisingly, high formation current promotes synchronized SEI growth, leading to a more uniform SEI coverage. Building on this mechanistic insight, we designed a pulsed high-current formation protocol for 2 Ah $LiFePO_4$ (LFP)/graphite pouch cells, achieving nearly an order-of-magnitude reduction in formation time while simultaneously enhancing the cycling performance. These findings challenge the prevailing belief that low currents are essential for developing a uniform SEI and pave a path toward safer and more efficient large-scale battery production.

battery | formation | operando microscopy | solid electrolyte interphase

Significance

The solid electrolyte interphase (SEI) governs the performance, lifetime, and safety of lithium-ion batteries (LIBs), yet its formation dynamics have remained unresolved due to its nanometric thickness and reactivity. Using operando optical microscopy, we directly visualize SEI nucleation, lateral propagation, and current-dependent evolution on graphite electrodes in real time. We find that high formation currents synchronize SEI growth, producing thinner and more uniform interphases. Guided by this mechanistic insight, we design rapid, high-current formation protocols that reduce formation time enhancing cycling stability. This work establishes a direct mechanistic link between formation conditions and interphase uniformity, providing guidance for efficient and safe battery manufacturing.

The growing demand for lithium-ion batteries (LIBs) underscores the importance of improving production throughput and ensuring manufacturing safety. A major challenge in large-scale battery production is optimizing the battery formation process, which accounts for nearly one third of battery manufacturing costs (1). Central to this process is the development of solid electrolyte interphase (SEI), a passivation layer formed on graphite from electrolyte decomposition. The SEI regulates capacity loss, cycle life, rate performance, and safety, making its control essential for large-scale battery production (2, 3).

Despite extensive studies using scanning and transmission electron microscopy (SEM/TEM) (4), X-ray Photoelectron Spectroscopy (XPS) (5), Raman spectroscopy (6), and more recently cryogenic Transmission Electron Microscopy (cryo-TEM) (7, 8) and synchrotron-based pair distribution function (PDF) (9), our understanding remains fragmentary. Most measurements are ex situ and provide only static snapshots that do not represent behavior in a realistic working cell, leaving the dynamic nucleation, growth, and evolution of the interphase unresolved (10). To uncover the underlying mechanisms, in situ or operando methods under realistic electrochemical conditions are required. Yet such approaches remain scarce, due to technical challenges associated with the nanometric thickness of the SEI, its chemical fragility, and the difficulty of integrating sensitive probes into a realistic working cell, leaving the kinetic processes underlying SEI growth poorly understood (11–13).

This knowledge gap is particularly consequential for the initial formation step of LIBs. Conventionally, formation is conducted under slow, low-current charging conditions to avoid nonuniform SEI growth (14, 15). However, industrial pressures toward faster, more efficient formation have revived interest in high-current protocols (16). Recent studies suggest that high-current formation could potentially yield SEI layers that are thinner, denser, and richer in inorganic species, thereby enhancing Li^+ transport and improving cycling durability (17). However, the mechanistic picture remains incomplete, and how current density dictates SEI nucleation and growth is not resolved. Without a comprehensive mechanistic understanding of how current density influences SEI dynamics, the optimization of formation strategies remains empirical and limited.

Here, we directly visualize SEI formation on graphite anodes using reflection-mode optical microscopy, exploiting the SEI-induced refractive-index matching effect. The imaging result reveals pronounced lateral heterogeneity and asynchronized reaction-front propagation during the first lithiation. Remarkably, higher formation currents synchronize SEI growth and suppress the lateral heterogeneity, challenging the conventional reliance on slow, low-current formation. Building on this insight, we develop a pulsed high-current

Author contributions: K.Z., G.Y., and Y.L. designed research; W.L. and S.R.S. performed research; W.L., T.S., Z.J., and J.Z. analyzed data; and W.L., S.R.S., K.Z., G.Y., and Y.L. wrote the paper.

Competing interest statement: The authors are working with UT Austin's patent office on the filing.

This article is a PNAS Direct Submission.

[1]W.L., T.S., and S.R.S. contributed equally to this work.

[2]To whom correspondence may be addressed. Email: kjzhao@purdue.edu, ghyu@austin.utexas.edu, or liuyijin@utexas.edu.

This article contains supporting information online at https://www.pnas.org/lookup/suppl/doi:10.1073/pnas.2531794123/-/DCSupplemental.

Published March 3, 2026.

protocol that shortens the initial formation charge from 10 to 20 h to 1 to 2 h while enhancing capacity retention. These findings establish a mechanistic basis for SEI control and highlight a path toward faster, safer, and more scalable battery manufacturing.

Results and Discussion

Asynchronous and Heterogeneous SEI Formation in Graphite Anodes During the First Lithiation. During the initial lithiation on the graphite electrode, the electrolyte solvents and salt anions are reduced to generate insoluble inorganic and organic species that deposit on the electrode surface as the SEI, when their last unoccupied molecular orbital (LUMO) levels lie below the Fermi level of the graphite electrode (18). This process gradually modifies the interfacial optical properties of the graphite. Specifically, before SEI formation, the large difference in refractive indices of the electrolyte (1.4) (19) and graphite (2.7) (20) yields a strong interface reflection. Once a thin SEI layer is developed, its refractive index (1.5) partially bridges this gap, thereby reducing the reflectivity. Notably, this reflectance reduction is governed by refractive-index matching rather than the specific chemical identity of SEI components. Most inorganic and organic SEI species exhibit refractive indices within a relatively narrow range (≈1.4 to 1.6), intermediate between the electrolyte and graphite, leading to a consistent optical darkening. This process is illustrated in Fig. 1*A* and discussed further in *SI Appendix*, section 1. We exploit this refractive index matching effect as a sensitive optical probe to track the dynamic formation and evolution of the SEI. To implement this under realistic conditions, we developed an operando optical microscopy method based on a modified 2016-type coin cell with a transparent optical window (*SI Appendix*, Fig. S5). This configuration enables direct visualization of the graphite electrode in a working cell, more faithfully replicating practical battery conditions than the open-cell setups previously used for optical studies of cathode (21) and anode (22, 23) electrodes. The cell consists of a graphite working electrode, a lithium metal counterelectrode, and a separator. The optical microscope with a long-working-distance objective lens was operated in reflection mode, allowing the detection of subtle changes on the graphite surface. The intensity of the optical images serves as an indicator of SEI formation and evolution, which will be elaborated and validated in the next section.

Optical images of the graphite electrode were recorded with one-minute intervals throughout the entire first lithiation at C/10 (over the course of 10 h). A few key frames were selected for further analysis here. First, there is a notable image intensity

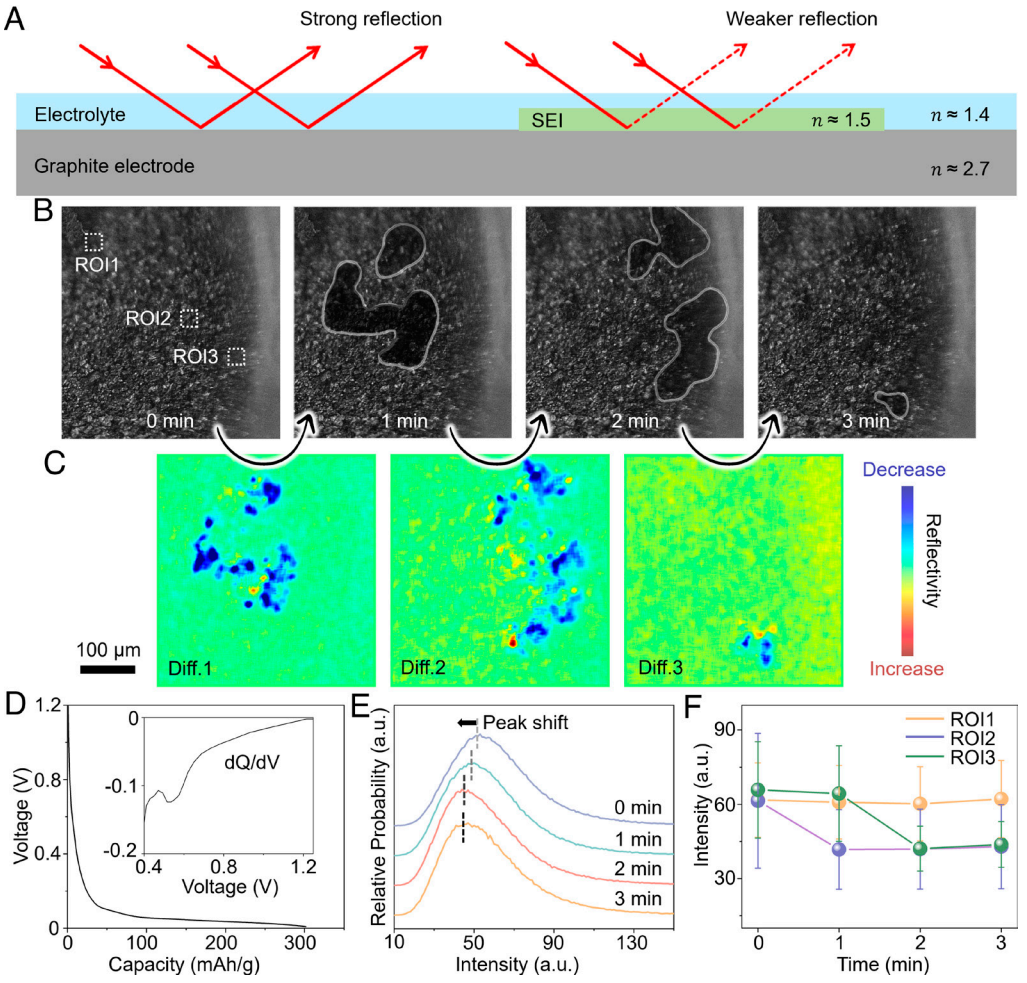

Fig. 1. Visualizing the SEI formation dynamics in a graphite electrode with operando optical microscopy. (*A*) Schematic illustration of the refractive index matching effect. (*B*) The graphite electrode surface imaged using optical microscopy during the first lithiation. (*C*) Sequential differential maps reveal active regions on the graphite electrode's surface over the corresponding time window. (*D*) Electrochemical data for the graphite/Li metal half-cell's first lithiation at C/10. Differential capacity (dQ/dV, unit of mAh/V) vs voltage is displayed in the insets. (*E*) Evolving image intensity histogram of the graphite surface. (*F*) Intensity evolution over three regions of interest as annotated in panel *B*.

change upon lithiation (Fig. 1 *B* and *E*), and it clearly demonstrates a sequential propagation with irregularly shaped patterns (Fig. 1*B*). To better visualize these data, Fig. 1*C* shows active regions by displaying the differential intensity maps (Diff.1, Diff.2, and Diff.3). These differential intensity maps were computed by analyzing pixel-wise intensity changes between two consecutive image frames, visually demonstrating the highly localized nature of the SEI formation process and revealing pronounced spatial heterogeneity. Blue regions indicate an intensity decrease upon SEI development. Green regions show negligible change, indicating little to no active reactions over the corresponding area and time window. These visual assessments are corroborated using the intensity histograms of the images. As lithiation progresses, the intensity probability distribution in Fig. 1*E* shifts toward lower values, indicating a decline in reflectance.

Three regions of interest (ROI1, ROI2, and ROI3 in Fig. 1*B*) were selected to monitor localized intensity change and analyze the temporal progression of reaction kinetics across the graphite electrode (Fig. 1*F*). While ROI1 remains largely unchanged throughout the selected 3-min time window, ROI2 experiences a clear intensity drop after 1 min, marking the onset of electrochemical reactions in the imaged field of view. By the 2-min mark, ROI3 exhibits significant changes, indicating a delay in its chemical and electrochemical reactions. These results confirm that reactions across the graphite electrode do not occur uniformly or simultaneously but follow distinct spatial and temporal patterns.

The onset of image darkening occurs at ~0.5 V, coinciding with a clear dQ/dV peak at 0.54 V (Fig. 1*D*) that is attributed to the reduction of EC and the generation of SEI species and precursors depositing on the graphite surface (24). The optical reflectivity reduction is clearly not related to the state of charge (SOC) because it only takes place during the first lithiation and is irreversible as we monitored the graphite electrode over several charge and discharge cycles (*SI Appendix*, Fig. S8). In addition, this phenomenon is clearly driven by electrochemical reactions as no change was observed in a control cell that was not subjected to the charging current (*SI Appendix*, Fig. S9).

Surface Chemical Transformations Correlated with Optical Reflectivity Reduction. To complement our operando observations and to validate SEI formation as the chemical origin of the optical reflectivity reduction, we conducted ex situ analyses of the graphite electrode surface before and after the first lithiation. Scanning electron microscopy (SEM) and energy-dispersive X-ray spectroscopy (EDX) were employed to investigate the surface composition of graphite electrodes before and after the first lithiation to 0.01 V. As shown in the SEM images (Fig. 2 *A* and *E*), the morphologies of the graphite electrode are similar before and after the first lithiation. EDX elemental mapping (Fig. 2 *B–D*) reveals that phosphorus (P) and fluorine (F) are codistributed on the surface of the pristine graphite electrode, indicating that the lithium salt ($LiPF_6$) adheres to the electrode surface without significant decomposition. The spatial correlation analysis (Fig. 2*I*) further supports the colocalization of P and F, suggesting the preservation of the electrolyte components. In contrast, after the first lithiation, the P and F distributions become spatially decoupled (Fig. 2 *F–H*), implying decomposition of the electrolyte and the formation of new compounds on the graphite surface. The statistical correlation analysis (Fig. 2 *I* and *J*) further confirms this transformation, with a strong correlation (PPMCC = 0.78198) in the pristine state, which decrease significantly (PPMCC = 0.38328) after lithiation, highlighting the electrolyte decomposition process during the initial lithiation.

Further, we conducted XPS measurements on the graphite samples to analyze the variations in their surface chemistry. Fig. 2 *K–N* present high-resolution XPS profiles of C 1*s*, O 1*s*, F 1*s*, and P 2*p* for the two graphite samples. In the pristine graphite sample, the C 1*s* spectrum (Fig. 2*K*) exhibits a prominent peak at ~284.0 eV, characteristic of graphite, along with contributions from weakly adsorbed surface species, including aliphatic peak C–C/H (~284.8 eV), C–O (~286.7 eV), and O–C=O (~289.0 eV) (25). The O 1*s* spectrum (Fig. 2*L*) shows a dominant peak at ~533.2 eV, attributed to C–O species (26), indicating the presence of weakly adsorbed oxygen-containing compounds on the surface. The F 1*s* spectrum (Fig. 2*M*) presents distinct peaks associated with the PVDF binder (~688.5 eV) and residual $LiPF_6$ from electrolyte exposure (~686.5 eV) (27, 28). Meanwhile, the P 2*p* spectrum (Fig. 2*N*) predominantly displays signals originating from $LiPF_6$ with a small contribution from the other phosphate species (29). The XPS analysis of the pristine graphite sample reveals both the intrinsic properties of the graphite electrode and the residual lithium salts from electrolyte.

After the initial lithiation process, significant changes in the surface composition are observed on the graphite electrode. In the C 1*s* spectrum (Fig. 2*K*), the characteristic graphite peak at ~284.0 eV is diminished, accompanied by the emergence of a new peak at ~282.2 eV, which is attributed to Li–C bonding environments, possibly corresponding to lithium carbides (30), indicating the replacement of the pristine graphite signal by SEI-related species during the first lithiation. Simultaneously, a distinct peak emerges at ~290.0 eV and a corresponding peak at ~531.9 eV in the O 1*s* spectrum (Fig. 2*L*), which is characteristic of carbonate species and can be assigned to Li_2CO_3 as well as organic lithium carbonates such as $ROCO_2Li$, both of which are typical SEI components (31). Beyond the carbonate contribution, the O 1*s* spectrum exhibits additional peaks at ~530.5 eV and ~527.9 eV, which correspond to LiOH and Li_2O, respectively (32). The presence of these oxygen species highlights the progressive development of the SEI, primarily originating from the decomposition of EC. The F 1*s* spectrum (Fig. 2*M*) undergoes a notable transformation, where the PVDF peak (~688.5 eV), initially present in the pristine sample, disappears after the lithiation. This disappearance, along with the suppression of the graphite signal in the C 1*s* spectrum, suggests that the surface of the graphite electrode is now covered with SEI. Meanwhile, a pronounced peak emerges at ~684.9 eV, corresponding to LiF (32), a key inorganic component of the SEI, formed through electrolyte solvent decomposition and lithium salt degradation.

The ex-situ analyses reveal surface chemical transformations consistent with our operando optical observations. The SEI formed during the first lithiation progressively covers the graphite electrode with species such as LiF, LiOH, and Li_2O, which alter the interfacial reflectivity and account for the image darkening and spatially heterogeneous optical contrast observed in reflection-mode microscopy.

Current-Dependent SEI Formation Kinetics. The formation of SEI during the initial lithiation of graphite electrode exhibits significant lateral heterogeneity. This heterogeneity primarily arises from variations in local electrochemical reaction rates, leading to nonuniform accumulation of electrolyte decomposition products. As SEI formation progresses, regions with faster reaction kinetics experience more extensive electrolyte decomposition, resulting in localized variations in composition, structure, and thickness (33). Understanding and manipulating these spatial heterogeneities is crucial for optimizing SEI properties and improving lithium-ion battery performance. Formation current density significantly influences SEI growth by dictating the rate of electrochemical

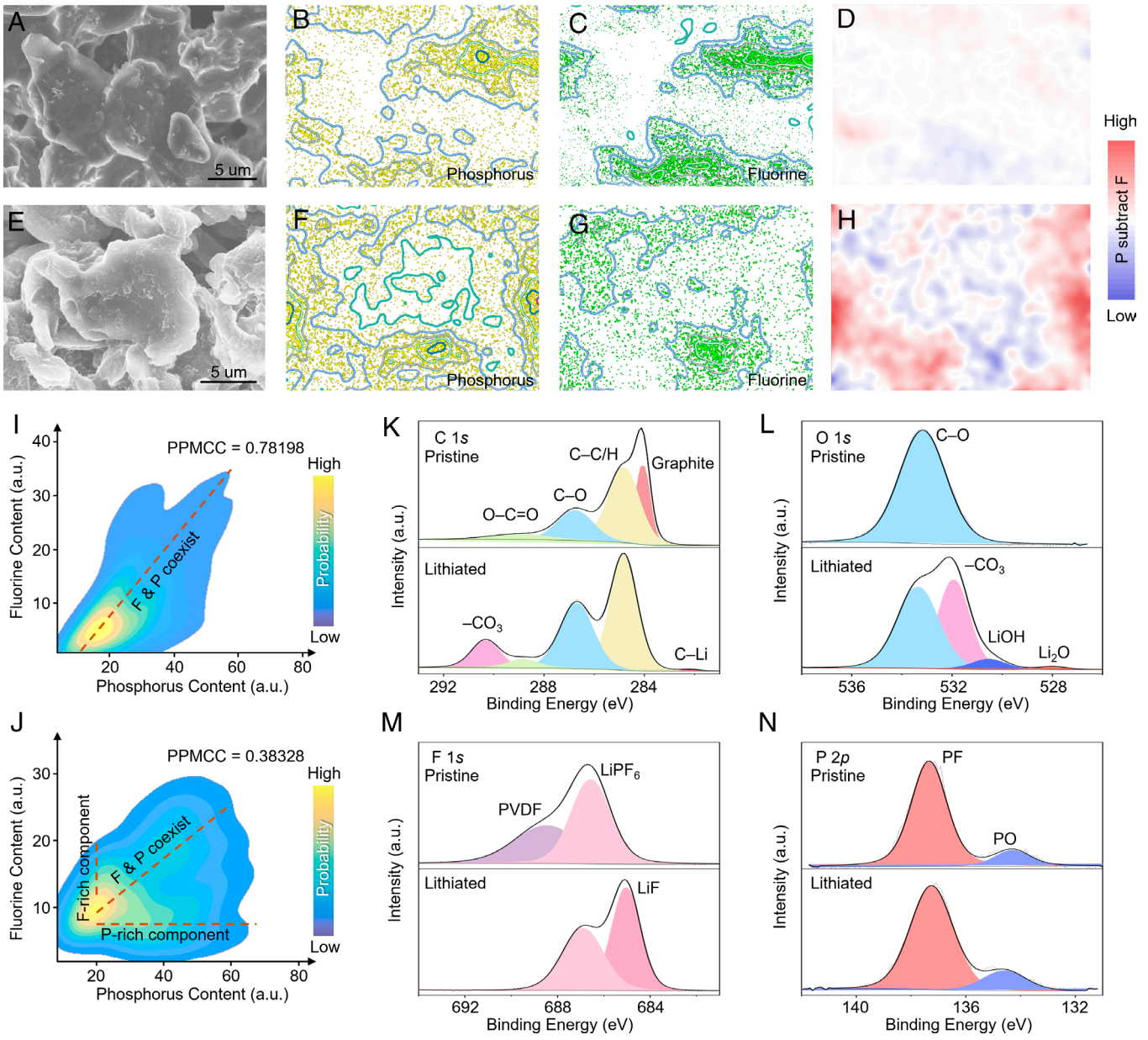

Fig. 2. Characterization of surface chemical transformations of graphite electrode during the first lithiation. (*A*), SEM image of pristine graphite electrode before the first lithiation. (*B* and *C*) EDX elemental mapping for P (*B*) and F (*C*) over the pristine electrode. (*D*) Spatial correlation analysis of F and P in the pristine graphite electrode. (*E*) SEM image of graphite electrode after the first lithiation to 0.01 V. (*F* and *G*) EDX elemental mapping for P (*F*) and F (*G*) over the lithiated graphite electrode. (*H*) Spatial correlation analysis of F and P in the lithiated graphite. (*I* and *J*) Statistical correlation analysis of F and P in the graphite electrode before (*I*) and after (*J*) the first lithiation. (*K*–*N*) Comparison of XPS profiles of C 1*s* (*K*), O 1*s* (*L*), F 1*s* (*M*), and P 2*p* (*N*) for graphite electrodes before and after the first lithiation.

reactions and the nature of the resulting deposits. To further elucidate how current density influences the SEI formation process, we conduct operando optical imaging with varying charging currents.

We compare SEI formation kinetics during the first lithiation under three different charging currents, C/20, C/10, and 1C (electrochemical data shown in *SI Appendix*, Fig. S15). Figs. 3 *A*–*C* shows sequential differential maps reconstructed from the raw imaging data by subtracting the preceding frame at each time point to highlight lithiation current-induced changes. Initially, the graphite surface is uniform with no detectable SEI coverage. As lithiation proceeds, heterogeneous SEI formation becomes evident, appearing as darkened regions in the raw data. At C/20 (Fig. 3*A*), localized SEI development progresses sequentially and intermittently, with discrete reaction front propagation appearing over an extended timescale. At C/10 (Fig. 3*B*), SEI nucleation initiates near-simultaneously at several discrete locations, indicative of rapid and spatially distributed growth. Under the higher current of 1C (Fig. 3*C*), a greater number of reactive sites are activated, with SEI formation occurring concurrently across broader surface regions. These observations suggest that increasing current not only accelerates SEI propagation but also promotes a more extensive spatial distribution of reactive events. The final panel in each sequence captures the spatiotemporal evolution of SEI coverage, revealing the dynamic propagation (indicated by different contour transparency) of reactive regions (indicated by different contour colors). A more detailed view of these localized spatiotemporal dynamics is provided in *SI Appendix*, Figs. S12–14, which extract individual regions from the final contour maps and highlight the sequential evolution of SEI growth at different

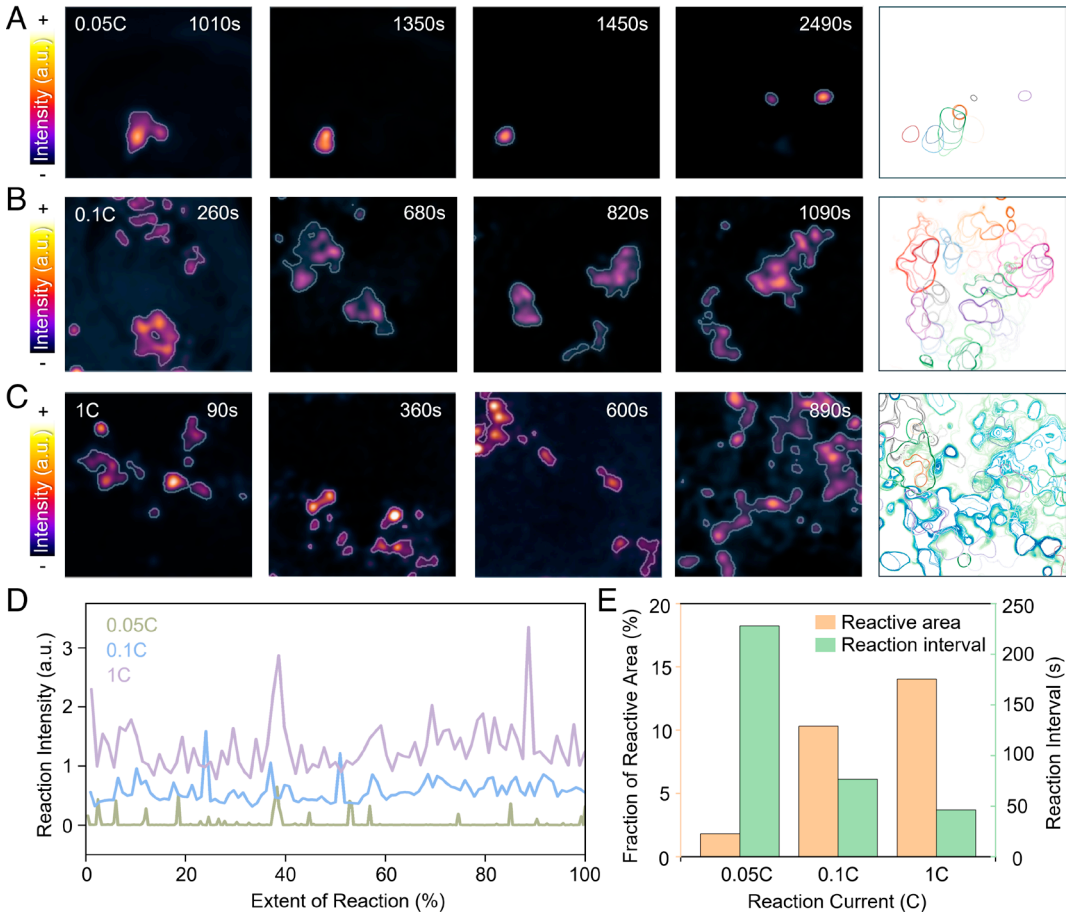

Fig. 3. Spatiotemporal evolution of SEI formation on graphite electrodes under different charging currents. (*A*) Sequential differential maps and SEI coverage evolution of a graphite/Li metal half-cell at C/20. (*B*) Sequential differential maps and SEI coverage evolution of a graphite/Li metal half-cell at C/10. (*C*) Sequential differential maps and SEI coverage evolution of an $LiFePO_4$ (LFP)/graphite full cell under pulsed current structures at 1C. (*D*) Reaction intensity profiles over the course of the first formation charge under varying currents. e, Average reactive area and temporal interval between sequential SEI formation events.

currents, with the complete dynamics captured in real time in Movies S1–S3. Compared to the C/20 current, where SEI growth tends to proceed through isolated events over time, higher current densities give rise to a greater number of coevolving reaction fronts, suggesting that SEI formation occurs independently and concurrently across multiple regions. To quantitatively evaluate the kinetics of SEI formation under different current densities, we analyzed the temporal evolution of reaction intensity and spatial coverage. As shown in Fig. 3*D*, reaction intensity profiles derived from differential maps reveal discrete SEI formation events under small charging current (C/20), marked by peaks that correspond to local reaction bursts. Increasing the current leads to higher peak intensities and shorter intervals between successive events, suggesting more frequent and spatially distributed SEI growth. The average interval between reaction peaks decreases from 228 s at C/20 to 77 s at C/10 and 46 s at 1C (Fig. 3*E*). Concurrently, the spatial extent of reactive regions increases significantly, as shown in Fig. 3*E*, with the fraction of reactive area (compared to whole imaged area) rising from < 2% at C/20 to ~10% at C/10 and ~18% at 1C. These results highlight the accelerating effect of higher current on both the frequency and spatial spread of SEI formation across the electrode surface.

This difference in reaction kinetics suggests that higher current densities promote concurrent and more evenly distributed SEI growth, whereas lower current densities lead to sequential and localized SEI formation, occurring at different times across the electrode. Traditionally, low formation current is believed to promote homogeneous lithiation, leading to a dense and uniform SEI. However, our experimental results reveal a contrasting trend, where higher current appears to facilitate more synchronized SEI development. This unexpected finding suggests a perspective on formation protocol optimization, where higher current may be beneficial if managed properly.

Finite Element Insights into SEI Nucleation and Growth. To elucidate the influence of formation current on SEI, we developed a multiphysics finite element model that couples electrochemical reactions, nucleation barriers, and transport dynamics to capture the spatiotemporal evolution of SEI nucleation and growth on graphite electrodes. The model explicitly accounts for the electrolyte reduction reactions occurring once the anode potential exceeds the electrolyte LUMO, leading to the formation of reduction products. The insoluble products undergo precipitation–nucleation on the graphite surface, overcoming the nucleation barrier ΔG_{nuc}, and progressively form SEI islands. As illustrated in the schematic (Fig. 4*A*), the model further resolves the subsequent expansion and coalescence of SEI islands, reproducing their transition from discrete nuclei to a continuous film. The central innovation is the introduction of a spatially dependent nucleation potential $E_{nuc}(X)$ into the SEI overpotential formulation, enabling the model to capture spatial heterogeneities associated with grain orientation, lithium content, and precursor nucleation dynamics that conventional models assuming a constant E_{SEI} overlooked.

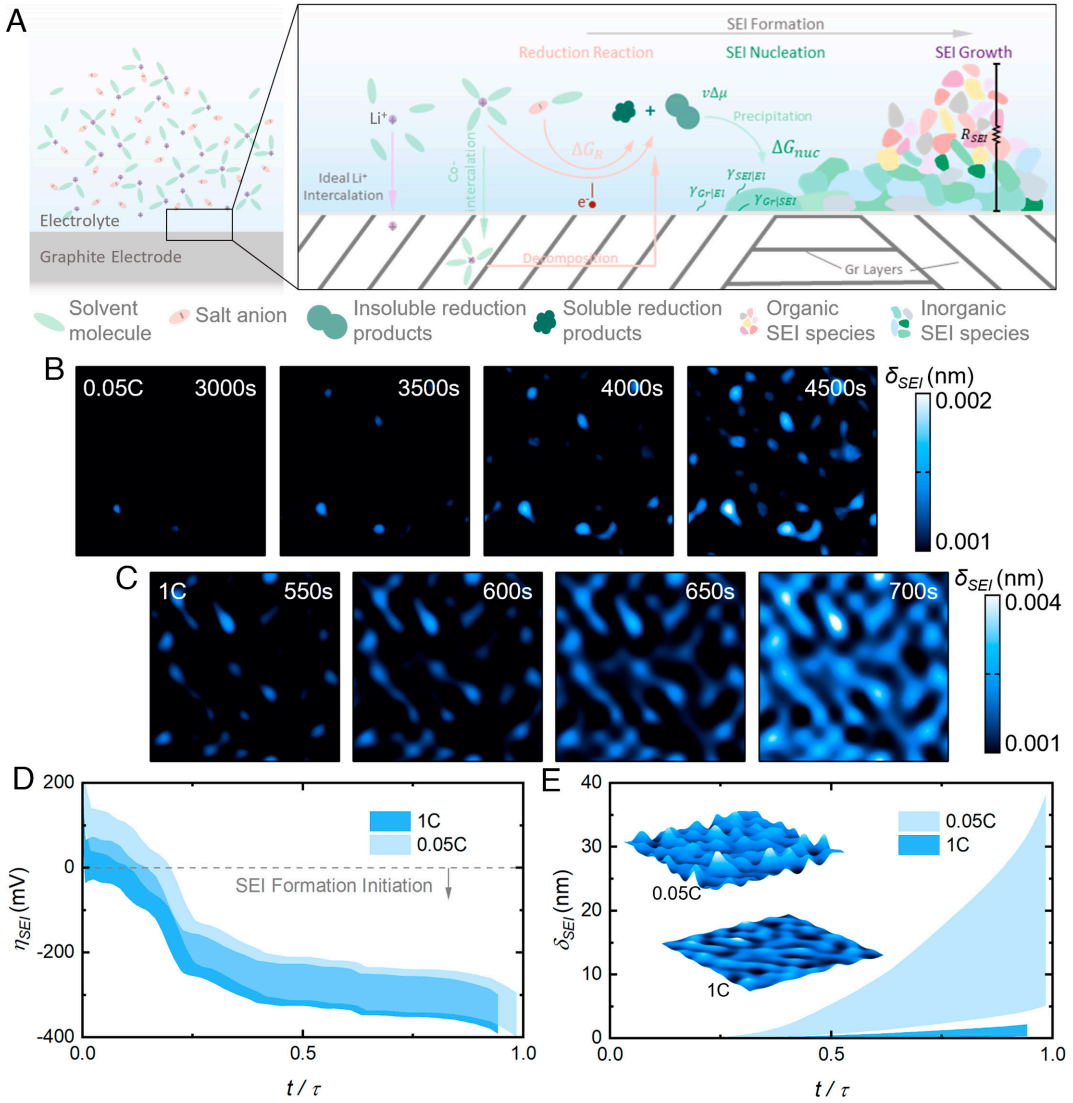

Fig. 4. Spatiotemporal variation of simulated SEI growth kinetics. (*A*) Schematic illustration of initial formation of SEI on graphite electrode surface. (*B*) Simulated SEI thickness evolution of a graphite/Li metal half-cell at C/20. (*C*) Simulated SEI thickness evolution of a graphite/Li metal half-cell at 1C. (*D*) Range of spatial variation in SEI formation overpotential, η_{SEI}, of a graphite/Li metal half-cell at C/20 and 1C. (*E*) Range of spatial variation in SEI thickness, δ_{SEI}, and 3D scaled render of SEI morphology, of a graphite/Li metal half-cell at C/20 and 1C.

Fig. 4 *B* and *C* show the spatiotemporal changes in SEI layer thickness δ_{SEI} over a 100 μm × 100 μm graphite electrode surface at C/20 and 1C currents, respectively. At low current (C/20), SEI islands emerge sporadically and progressively in localized regions, resulting in significant delays, whereas at high current (1C), multiple SEI islands nucleate rapidly and concurrently, quickly merging into a continuous SEI layer with much greater spatial uniformity. The variation of SEI overpotential, η_{SEI} is shown in Fig. 4*D*. The shaded plot represents the spatial variation of η_{SEI}. Numerically, SEI formation initiates when η_{SEI} drops below 0 mV, which can be physically interpreted as the overcoming of the reduction and nucleation energy barriers. At C/20 formation rate, η_{SEI} remains positive over the entire electrode surface for a significant initial time period, indicating unfavorable conditions for SEI formation. η_{SEI} is negative over some regions of the electrode surface almost instantaneously with the application of 1C charging current, indicating an almost simultaneous inception of SEI nucleation. By 525 s, the entire electrode surface presents favorable conditions for SEI formation, while it takes 14,000 s for this to occur with C/20 charging rate. Slow charging rate of C/20 encourages a much thicker SEI layer than 1C (Fig. 4*E*). Interestingly, the initial SEI formation influences the structure of SEI layer at the end of formation. The spatiotemporal inhomogeneity in SEI formation at C/20 results in a large variation in SEI thickness, varying from 5.2 nm to 38 nm across the electrode surface. 1C charging rate results in a thinner, relatively uniform SEI layer, with thickness varying from 0.33 nm to 2.2 nm. The difference in SEI layer morphology is evident in the inset images in Fig. 4*E* that depict the rendered SEI surface at the end of first lithiation. The simulation captures the current-dependent SEI formation kinetics observed in our experiments. Faster current enables a larger surface area to overcome SEI formation and nucleation energy barrier allowing multiple SEI islands to emerge concurrently, while under slower formation current the energy barrier is overcome sequentially over the electrode surface.

LIBs Formation under Pulsed High Charging Current. Building on the finding that higher current fosters more synchronized SEI developments across the electrode, we next examine the impacts of high-current battery formation strategies using $LiFePO_4$ (LFP)/graphite full cells. The designed testing protocol is shown in Fig. 5*A*. The formation protocol involves first

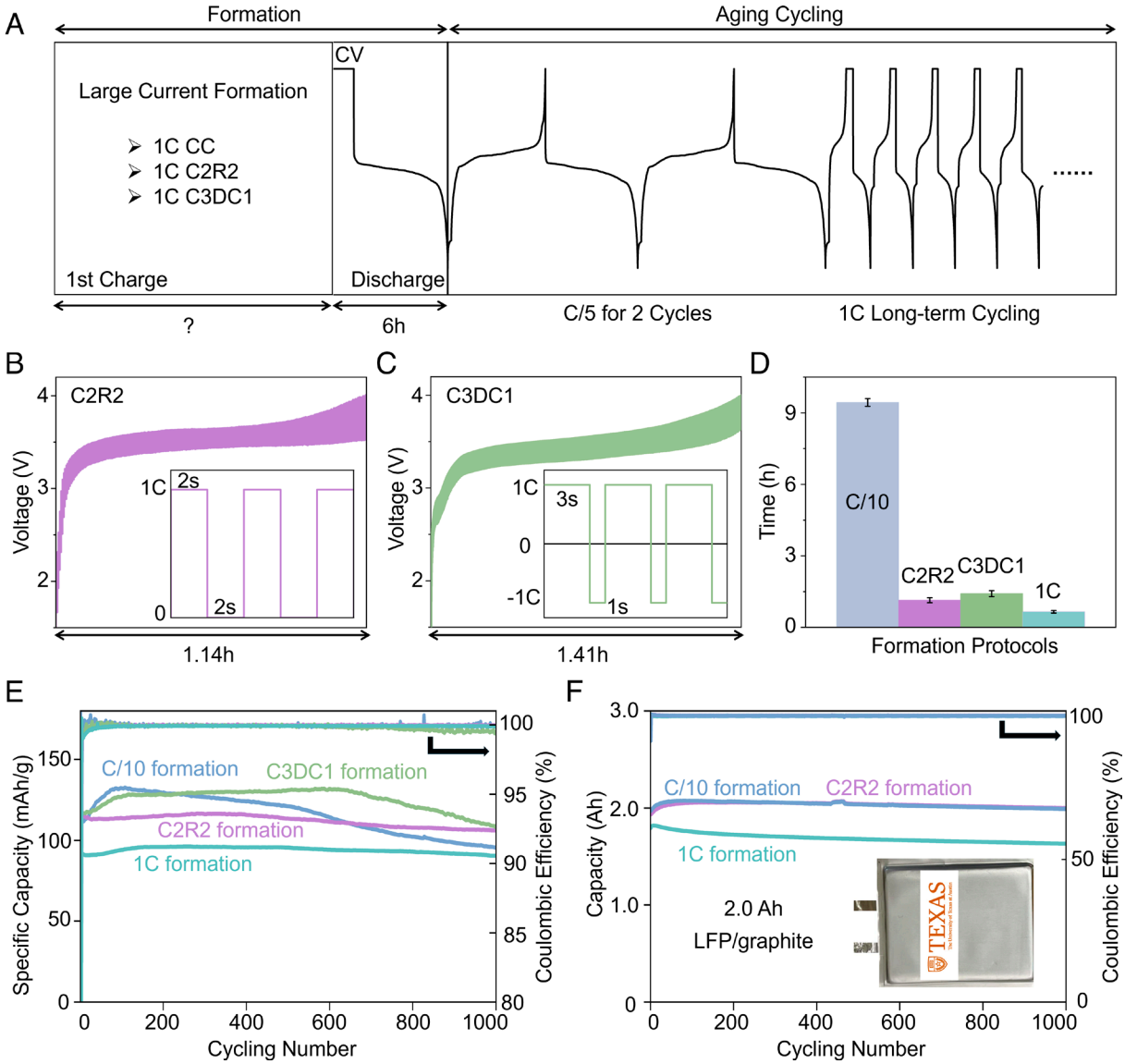

Fig. 5. High-current formation protocol design and analysis. (*A*) Formation and aging cycling scheme. (*B*) C2R2 first-cycle formation charging voltage curve and its pulsed current structure. (*C*) C3DC1 first-cycle formation charging voltage curve and its pulsed current structure. (*D*) The formation time (i.e., the initial lithiation time) for all the formation protocols in LFP/graphite coin cells. (*E*) Electrochemical performances of LFP/graphite coin cells with different formation protocols. (*F*) Electrochemical performances of 2 Ah LFP/graphite pouch cells with different formation protocols.

charging the battery to 4.0 V at 1C, followed by a 1-h constant voltage (CV) hold at 4.0 V. However, 1C charging also induces a strong polarization, which can compromise the uniformity in the out-of-plane direction (34, 35). Given that pulsed charging currents have been shown to alleviate polarization (36, 37), we introduced two pulsed current structures for the initial formation charge: C2R2 (1C charge for 2 s, followed by a 2-s rest, Fig. 5*B*) and C3DC1 (1C charge for 3 s, followed by a 1-s discharge, Fig. 5*C*). In C2R2, the rest period primarily relaxes transport-induced polarization, whereas in C3DC1 the brief discharge transiently resets the interfacial overpotential. After the initial 1C charge with a CV hold and subsequent C/5 discharge to 2.5 V, the formal formation step was completed. The cells were then subjected to an aging protocol at room temperature (RT), which began with two additional C/5 cycles between 2.5 and 4.0 V without the CV hold, followed by long-term cycling at 1C. Each 1C aging cycle consisted of charging to 4.0 V with a CV hold until C/20, followed by a 1C discharge to 2.5 V. For comparison, a control group is prepared, employing a constant current (CC) protocol at C/10 for the first formation charge, with all other steps unchanged.

We first validated this approach in LFP/graphite coin cells and subsequently extended it to 2 Ah LFP/graphite pouch cells. One straightforward effect of the developed high-current formation is the shortened first cycle charging time (Fig. 5*D*), which decreases significantly from 9.44 h for C/10 to 0.66 h for 1C. The formation time of the C2R2 and C3DC1 protocols with pulsed current structures is slightly longer than that of 1C CC but remains on the same order of magnitude, significantly shorter than the 9.44 h required at C/10. Fig. 5*E* shows the cycling performance of LFP/graphite coin cells at RT at a 1C charge/discharge rate. Notably, all the cells exhibited a slight increase in capacity during the first 200 cycles. This capacity increase may be attributed to the micro-cracking of the LFP particles, which increases surface area and shortens diffusion path lengths (38). All the tested LFP/graphite cells exhibited excellent capacity retention, although the cells activated with 1C CC protocol demonstrate a lower capacity. Batteries activated with the C3DC1 and the C/10 CC protocols showed

similar cycling performance, with capacity beginning to decline after more than 600 cycles but still maintaining a capacity retention rate above 90%. In contrast, batteries activated with the C2R2 protocol demonstrated the best cycling stability, retaining over 90% of the initial capacity after 1,000 cycles. This superior performance can be attributed to the SEI formed under pulsed high-current conditions, which is thinner, more uniform, and enriched in LiF, thereby lowering SEI interfacial impedance, as confirmed by XPS and electrochemical impedance spectroscopy (EIS) analyses (*SI Appendix*, section 6.1). XPS further indicates that although the SEI across different protocols consistently comprises chemical species such as LiF, Li_2CO_3, and $ROCO_2Li$, their relative proportions differ significantly. After 1,000 aging cycles at 1C, SEM and XPS (*SI Appendix*, section 6.2) show that under the C/10 formation protocol the graphite surface exhibits pronounced nonuniform lithium deposition and accumulates solvent- and salt-derived decomposition products, indicating aggravated electrolyte side reactions, whereas under high-current formation the graphite surface remains more stable, retaining its original morphology. In pouch cells (2.0 Ah LFP/graphite), three formation protocols were compared: C/10, 1C, and 1C C2R2. As expected, the 1C protocols dramatically shortened the initial formation time, reducing it from more than 12 h at C/10 to less than 1 h at 1C (*SI Appendix*, Table S3). Notably, the pulsed 1C C2R2 protocol yielded the most balanced outcome, coupling a markedly reduced formation time with complete capacity retention over 1,000 cycles (Fig. 5*F*). Taken together, these results show that high-current pulse formation not only significantly reduces formation time, but also promotes the development of a thin, uniform, and robust SEI that improves interfacial uniformity and mitigates electrolyte parasitic reactions, thereby enhancing long-term cycling stability.

Conclusion

In this study, we leveraged the SEI-induced refractive index matching effect and employed operando optical microscopy to directly observe the SEI formation dynamics in graphite electrodes during the initial lithiation. Our findings revealed pronounced lateral SEI heterogeneity and asynchronous SEI evolution across the graphite electrode. Surprisingly, higher current densities facilitated concurrent local reactions, leading to a more synchronized SEI development across different regions. This observation challenges the conventional belief that low-current formation is essential for stable and uniform SEI development.

While high-current lithiation enhanced reaction uniformity in graphite electrode, it also introduced challenges such as increased polarization. To address this, we implemented pulsed high-current formation, which effectively mitigated polarization effects while accelerating SEI formation kinetics. This approach significantly reduced the first charging time from approximately 10 to 20 h to about 1 h, all while maintaining superior energy density and cycling stability.

While our results directly demonstrate improvements in cycling performance and production throughput, the potential impact of this method on manufacturing cost and safety warrants further elaboration. The battery formation process accounts for approximately one third of production-related costs due to its energy-intensive and time-consuming nature (1, 39). This is very significant given that typical profit margins for battery manufacturers range from 10 to 20% (40, 41). A battery assembly line can produce dozens of cells per minute (42, 43). However, these cells must be stored at elevated temperatures for tens of hours, even days, to undergo the formation process. The risk of fire is very considerable, and the consequence is very significant, as seen in incidents like the fire at SK On's Georgia factory in 2024, which led to a $31 million settlement (44, 45). With significantly reduced formation time, our method could contribute to enhanced battery performance, production throughput, manufacturing cost efficiency, and safety.

Materials and Methods

Materials Preparation. Lithium metal chips (16 mm in diameter, 0.6 mm in thickness) were purchased from MTI Corporation (USA), while graphite and $LiFePO_4$ (LFP) electrodes were obtained from Canrud Technology Co., Ltd. The graphite electrode had a coating mass loading of 5.8 mg cm^{-2}, an active material fraction of 95.7%, and a specific capacity of 340 mAh g^{-1}. The LFP electrode had a coating mass loading of 12.3 mg cm^{-2}, an active material fraction of 91.5%, and a specific capacity of 150 mAh g^{-1}. The electrolyte was 1 M lithium hexafluorophosphate ($LiPF_6$) dissolved in ethylene carbonate (EC) and diethyl carbonate (DEC) (1:1 by volume), and the separator was a microporous polypropylene (PP) membrane (25 μm, Neware Technology Co., Ltd.). For coin-cell experiments, all cells were assembled using the above electrodes, PP separators, and electrolyte.

Operando Optical Experiments. In-situ optical experiments were conducted using a modified 2016-type coin cell with a transparent glass window, observed under an Olympus BX51 microscope coupled to a BioLogic VMP3 workstation for simultaneous electrochemical control (*SI Appendix*, section 2). Images were acquired at 10× or 20× objectives every 10 s or 1 min, enabling continuous monitoring over tens of hours. Measurements were performed on graphite/Li metal half-cells (under C/20 and C/10 currents, 0.01 to 2 V) and LFP/graphite full cells (under 1C current, 2.5 to 4.0 V), with imaging always focused on the graphite electrode surface.

Surface Chemical Characterization. SEM and EDX were performed on a Thermo Scientific Scios 2 SEM equipped with an EDX detector. Elemental P and F mapping was analyzed using the open-source software Image J, enabling contour, spatial correlation, and statistical correlation analyses.

XPS was conducted on a Kratos Axis Ultra DLD spectrometer (Kratos Analytical, Inc.) equipped with a monochromatic Al Kα X-ray source (120 W). Photoelectrons were collected at a 90° emission angle from a 300 μm × 700 μm area. High-resolution spectra were acquired in constant-analyzer-energy (CAE) mode with a pass energy of 20 eV and a step size of 0.1 eV, giving a full width at half maximum (FWHM) of 0.77 eV for the Ag $3d_{5/2}$ peak. The base pressure in the analysis chamber was maintained at ~5 × 10^{-9} Torr. High-resolution XPS spectra were deconvoluted using CasaXPS Version 2.3.26, with all binding energies calibrated against the adventitious C 1*s* peak at 284.8 eV.

SEM/EDX and XPS characterizations were conducted on two types of graphite electrodes. The first type consisted of pristine graphite electrodes, which were soaked in the electrolyte described in the Materials Preparation section for 12 h without electrochemical lithiation. The second type consisted of lithiated graphite electrodes, which were obtained after the first lithiation to 0.01 V and correspond to the optically darkened regions observed during operando lithiation. To ensure consistent electrolyte exposure, the graphite electrodes used for lithiation were also soaked in the same electrolyte for 12 h prior to electrochemical lithiation. Before XPS measurements, no solvent rinsing was applied, to preserve electrolyte- and SEI-derived species and to maintain consistency with the operando optical observations before and after lithiation.

Electrochemical Measurements. Coin-type LFP/graphite cells (CR2032) were assembled using 14 mm diameter LFP cathodes and 12 mm diameter graphite anodes, corresponding to an N/P ratio of ~1.1. The electrolyte volume was precisely controlled at 50 μL per cell. To minimize interference from the cathode, the LFP material was preactivated before anode formation to establish a stable CEI layer. Specifically, LFP/Li cells were assembled and charged to 4.0 V at 1C, followed by a constant-voltage (CV) hold at 4.0 V with a cutoff current of C/20. The cells were then discharged at C/5 to 2.5 V, followed by two additional C/5 charge–discharge cycles between 2.5 and 4.0 V without the CV hold. After preactivation, the cells were disassembled in an Ar-filled glovebox, and the LFP cathodes were reassembled with graphite anodes into the LFP/graphite coin cells. The assembled cells were first charged at C/10 to 1.5 V, followed by a 4 h hold to mitigate copper current collector corrosion and enhance electrolyte wetting. Both

LFP/Li and LFP/graphite coin cells were tested at room temperature (RT) using Land CT2001A battery testers.

Dry 2 Ah LFP/graphite pouch cells (without electrolyte) were purchased from Li-Fun (Hunan) New Energy Technology Co., Ltd. Detailed parameters are provided in *SI Appendix*, Table S2. Prior to electrolyte filling, all cells were vacuum-dried at 80 °C for 24 h and then transferred into an Ar-filled glovebox for electrolyte injection and sealing. A total of 12 g of electrolyte, identical to that used in the coin-cell experiments, was injected into each 2 Ah pouch cell. The cells were subsequently sealed under a gauge pressure of −90 kPa and precharged to 1.5 V to prevent copper foil dissolution. After electrolyte filling, the pouch cells were rested for 48 h at RT to ensure complete wetting before testing. Electrochemical measurements were conducted at RT using a Neware battery testing system. The testing protocols for both coin cells and pouch cells are summarized in Fig. 5*A*. Each formation protocol was tested in duplicate to confirm reproducibility.

Finite Element Modeling of SEI Formation and Growth. An electrochemical-mechanical model is implemented for a graphite/Li metal half-cell. The transport of Li^+ ions in the electrolyte and conduction of electrons in the conductive phase are modeled using the porous electrode governing equations established within Newman model (46). At the graphite–electrolyte interface, Butler–Volmer kinetics simulate the dynamic charge transfer reaction. Chemical potential forms the thermodynamic driving force for diffusion of Li in graphite after intercalation (47). The nonlinear intercalation induced strains are modeled analogous to thermal strains. Mismatch strains due to gradients in Li concentration induce stresses in graphite. A linear elastic material stress–strain constitutive law is employed. The complete set of governing equations for the coupled electrochemical–mechanical model are described in our previous work (48, 49). As our primary focus is SEI formation and growth, for simplicity we omit the stress influences on chemical potential and interfacial charge transfer as these are expected to be negligible for graphite.

The irreversible side reactions leading to SEI formation are modeled with a cathodic Tafel equation. The SEI formation current density, i_{SEI} is evaluated as:

$$i_{SEI} = -i_{0,SEI}\ \exp\left(-\frac{\alpha F \eta_{SEI}}{RT}\right), \qquad [1]$$

where $i_{0,SEI}$ is the SEI reaction exchange current density, α is the cathodic charge transfer coefficient, F is the Faraday constant, R is the universal gas constant, and T is the absolute temperature. The SEI reaction overpotential, η_{SEI} takes the form

$$\eta_{SEI} = E - E_{SEI} - E_{nuc} - i_{SEI}R_{SEI}, \qquad [2]$$

where E is the electrode potential, E_{SEI} is the reduction potential for the electrolyte, and E_{nuc} accounts for the spatial variation in the SEI formation and nucleation energy barrier. R_{SEI} is the resistance across the SEI layer, proportional to the SEI thickness, δ_{SEI}:

$$R_{SEI} = \frac{\delta_{SEI}}{\kappa_{SEI}}, \qquad [3]$$

where κ_{SEI} is the conductivity of the SEI film. The rate of SEI thickness growth is directly dependent on the rate of SEI reaction:

$$\frac{d\delta_{SEI}}{dt} = \frac{i_{SEI}M_{SEI}}{nF\rho_{SEI}}, \qquad [4]$$

where M_{SEI} and ρ_{SEI} are the molar mass and density of the SEI film, respectively, and n is the number of electrons involved in the reaction.

Data, Materials, and Software Availability. All study data are included in the article and/or supporting information.

ACKNOWLEDGMENTS. Y.L. acknowledges the support from NSF under Grant No. CBET-2349665. G.Y. acknowledges the funding support from the Welch Foundation Award F-1861 and Norman Hackerman Award in Chemical Research. The work at Purdue was supported by NSF under Grant No. CBET-2349666.

Author affiliations: [a]Materials Science and Engineering Program and Walker Department of Mechanical Engineering, The University of Texas at Austin, Austin, TX 78712; [b]School of Mechanical Engineering, Purdue University, West Lafayette, IN 47907; and [c]General Motors Company, Warren, MI 48092

1. Y. Liu, R. Zhang, J. Wang, Y. Wang, Current and future lithium-ion battery manufacturing. *iScience* **24**, 102332 (2021).
2. L. Wang *et al.*, Identifying the components of the solid–electrolyte interphase in Li-ion batteries. *Nat. Chem.* **11**, 789–796 (2019).
3. S. J. An *et al.*, The state of understanding of the lithium-ion-battery graphite solid electrolyte interphase (SEI) and its relationship to formation cycling. *Carbon* **105**, 52–76 (2016).
4. C. Hou *et al.*, Operando observations of SEI film evolution by mass-sensitive scanning transmission electron microscopy. *Adv. Energy Mater.* **9**, 1902675 (2019).
5. B. Heidrich, L. Pritzlaff, M. Börner, M. Winter, P. Niehoff, Comparative X-ray photoelectron spectroscopy study of the SEI and CEI in three different lithium ion cell formats. *J. Electrochem. Soc.* **169**, 030533 (2022).
6. S. Hy, Y.-H. Chen, J.-Y. Liu, J. Rick, B.-J. Hwang, In situ surface enhanced raman spectroscopic studies of solid electrolyte interphase formation in lithium ion battery electrodes. *J. Power Sources* **256**, 324–328 (2014).
7. Y. Li *et al.*, Atomic structure of sensitive battery materials and interfaces revealed by cryo–electron microscopy. *Science* **358**, 506–510 (2017).
8. M. J. Zachman, Z. Tu, S. Choudhury, L. A. Archer, L. F. Kourkoutis, Cryo-STEM mapping of solid–liquid interfaces and dendrites in lithium-metal batteries. *Nature* **560**, 345–349 (2018).
9. Z. Shadike *et al.*, Identification of LiH and nanocrystalline LiF in the solid–electrolyte interphase of lithium metal anodes. *Nat. Nanotechnol.* **16**, 549–554 (2021).
10. K. Xu, Electrolytes and interphases in Li-ion batteries and beyond. *Chem. Rev.* **114**, 11503–11618 (2014).
11. S. Tan *et al.*, Unravelling the convoluted and dynamic interphasial mechanisms on Li metal anodes. *Nat. Nanotechnol.* **18**, 243–249 (2023).
12. H. Adenusi, G. A. Chass, S. Passerini, K. V. Tian, G. Chen, Lithium batteries and the solid electrolyte interphase (SEI)–progress and outlook. *Adv. Energy Mater.* **13**, 2203307 (2023).
13. E. Peled, S. Menkin, SEI: Past, present and future. *J. Electrochem. Soc.* **164**, A1703 (2017).
14. X. Cui *et al.*, Data-driven analysis of battery formation reveals the role of electrode utilization in extending cycle life. *Joule* **8**, 3072–3087 (2024).
15. S. S. Zhang, K. Xu, T. R. Jow, Optimization of the forming conditions of the solid-state interface in the Li-ion batteries. *J. Power Sources* **130**, 281–285 (2004).
16. D. L. Wood, J. Li, S. J. An, Formation challenges of lithium-ion battery manufacturing. *Joule* **3**, 2884–2888 (2019).
17. C. Zhong *et al.*, Rapidly-formed interphase facilitating fast-charging lithium-ion batteries. *ACS Energy Lett.* **10**, 4627–4635 (2025).
18. J. B. Goodenough, Y. Kim, Challenges for rechargeable Li batteries. *Chem. Mater.* **22**, 587–603 (2010).
19. A. Nedjalkov *et al.*, Refractive index measurement of lithium ion battery electrolyte with etched surface cladding waveguide bragg gratings and cell electrode state monitoring by optical strain sensors. *Batteries* **5**, 30 (2019).
20. X. Wang, Y. P. Chen, D. D. Nolte, Strong anomalous optical dispersion of graphene: Complex refractive index measured by picometrology. *Opt. Express* **16**, 22105–22112 (2008).
21. N. Sharma, L. S. d. Vasconcelos, S. Hassan, K. Zhao, Asynchronous-to-Synchronous Transition of Li Reactions in Solid-Solution Cathodes. *Nano Lett.* **22**, 5883–5890 (2022).
22. G. Feng *et al.*, Imaging solid–electrolyte interphase dynamics using operando reflection interference microscopy. *Nat. Nanotechnol.* **18**, 780–789 (2023).
23. T. Sun, R. Peng, W. Li, Y. Liu, Image registration for accurate electrode deformation analysis in operando microscopy of battery materials. *J. Synchrotron Radiat.* **32**, 417–423 (2025).
24. J. S. Gnanaraj, R. W. Thompson, S. N. Iaconatti, J. F. DiCarlo, K. M. Abraham, Formation and growth of surface films on graphitic anode materials for Li-ion batteries. *Electrochem. Solid-State Lett.* **8**, A128 (2005).
25. X. Chen, X. Wang, D. Fang, A review on C1s XPS-spectra for some kinds of carbon materials. *Fuller. Nanotubes Carbon Nanostruct.* **28**, 1048–1058 (2020).
26. S. Kundu, Y. Wang, W. Xia, M. Muhler, Thermal stability and reducibility of oxygen-containing functional groups on multiwalled carbon nanotube surfaces: A quantitative high-resolution XPS and TPD/TPR study. *J. Phys. Chem. C* **112**, 16869–16878 (2008).
27. S. Oswald, K. Nikolowski, H. Ehrenberg, Quasi in situ XPS investigations on intercalation mechanisms in Li-ion battery materials. *Anal. Bioanal. Chem.* **393**, 1871–1877 (2009).
28. R. A. Quinlan, Y.-C. Lu, Y. Shao-Horn, A. N. Mansour, XPS studies of surface chemistry changes of LiNi0. 5Mn0. 5O2 electrodes during high-voltage cycling. *J. Electrochem. Soc.* **160**, A669 (2013).
29. K. Hirata, T. Kawase, Y. Sumida, Electrode/electrolyte interface study of LiCoO2/graphite cell using carbonate-free electrolytes based on lithium bis (fluorosulfonyl) imide and sulfolane. *J. Electrochem. Soc.* **167**, 020518 (2020).
30. A. Schechter, D. Aurbach, H. Cohen, X-ray photoelectron spectroscopy study of surface films formed on Li electrodes freshly prepared in alkyl carbonate solutions. *Langmuir* **15**, 3334–3342 (1999).
31. K. Kanamura, S. Shiraishi, H. Takezawa, Z.-I. Takehara, XPS analysis of the surface of a carbon electrode intercalated by lithium ions. *Chem. Mater.* **9**, 1797–1804 (1997).
32. W. Yu *et al.*, Electrochemical formation of bis(fluorosulfonyl)imide-derived solid-electrolyte interphase at Li-metal potential. *Nat. Chem.* **17**, 246–255 (2025).
33. Y.-X. Yao *et al.*, Nucleation and growth mode of solid electrolyte interphase in Li-ion batteries. *JACS* **145**, 8001–8006 (2023).
34. D. Goers, M. E. Spahr, A. Leone, W. Märkle, P. Novák, The influence of the local current density on the electrochemical exfoliation of graphite in lithium-ion battery negative electrodes. *Electrochim. Acta* **56**, 3799–3808 (2011).
35. W. Märkle, C.-Y. Lu, P. Novák, Morphology of the solid electrolyte interphase on graphite in dependency on the formation current. *J. Electrochem. Soc.* **158**, A1478 (2011).
36. J. Guo *et al.*, Unravelling the mechanism of pulse current charging for enhancing the stability of commercial LiNi0. 5Mn0. 3Co0. 2O2/graphite lithium-ion batteries. *Adv. Energy Mater.* **14**, 2400190 (2024).

37. X. Huang *et al.*, Effect of pulsed current on charging performance of lithium-ion batteries. *IEEE Trans. Ind. Electron.* **69**, 10144–10153 (2022).
38. E. R. Logan *et al.*, The effect of $LiFePO_4$ particle size and surface area on the performance of $LiFePO_4$/graphite cells. *J. Electrochem. Soc.* **169**, 050524 (2022).
39. W. Li *et al.*, Sponge-inspired pressing approach to facilitate electrolyte wetting in li-ion pouch cells. *J. Electrochem. Soc.* **172**, 090528 (2025).
40. T. E. Lipman, *The Cost of Manufacturing Electric Vehicle Batteries* (Institute of Transportation Studies, University of California, 1999).
41. Z. Yang, H. Huang, F. Lin, Sustainable electric vehicle batteries for a sustainable world: Perspectives on battery cathodes, environment, supply chain, manufacturing, life cycle, and policy. *Adv. Energy Mater.* **12**, 2200383 (2022).
42. M. Lechner *et al.*, Cost modeling for the GWh-scale production of modern lithium-ion battery cells. *Comms. Eng.* **3**, 155 (2024).
43. W. Li *et al.*, Multimodal characterization of coating defects in graphite electrodes for lithium-ion batteries. *J. Electrochem. Soc.* **172**, 080523 (2025).
44. P. Sun, R. Bisschop, H. Niu, X. Huang, A review of battery fires in electric vehicles. *Fire Technol.* **56**, 1361–1410 (2020).
45. T. Shan, P. Zhang, Z. Wang, X. Zhu, Insights into extreme thermal runaway scenarios of lithium-ion batteries fire and explosion: A critical review. *J. Energy Storage* **88**, 111532 (2024).
46. J. Newman, K. E. Thomas-Alyea, *Electrochemical Systems* (John Wiley & Sons. Inc Publication, 2004).
47. F. Larche, J. W. Cahn, The interactions of composition and stress in crystalline solids. *JRNBS* **89**, 467 (1984).
48. S. R. Shah, L. S. Vasconcelos, K. Zhao, Computational modeling of electrochemomechanics of high-capacity composite electrodes in Li-ion batteries. *J. Appl. Mech.* **89**, 081005 (2022).
49. L. S. de Vasconcelos *et al.*, Chemomechanics of rechargeable batteries: Status, theories, and perspectives. *Chem. Rev.* **122**, 13043–13107 (2022).